Pubblicazioni del Centro De Giorgi
Proceedings of the Interdisciplinary Workshop on Mathematical Methods in Biomedical Imaging and Intensity-Modulated Radiation Therapy (IMRT), Pisa, Italy, October 2007.

Non-Contact Fluorescence Optical Tomography with Adaptive Finite Element Methods

Amit Joshi and Wolfgang Bangerth

Key words and phrases. Optical Tomography, Adaptive Finite Element Methods, Inverse Imaging Problems.

ABSTRACT. Fluorescence optical tomography is a rapidly expanding biomedical imaging modality, which exploits the deep penetration of near infrared light in tissue and molecularly targeting fluorescence agents, to locate diseased tissue regions in three dimensions. Mathematically, the fluorescence optical tomography problem is an inverse problem which involves the identification of coefficients of a coupled elliptic PDE system describing the propagation of NIR photons in tissue. The inverse optical tomography problem is typically cast as a nonlinear optimization problem and solved by Newton-type methods. However, the computational expense of repeatedly solving the coupled elliptic system for generating image updates restricts how fine a discretization of the partial differential equation can be employed. Further, since light rapidly attenuates by multiple scattering and absorption in tissue, the tomography problem for determining the concentration of a fluorescence agent in tissue is highly ill-posed, which also affects the choice of discretization level. In the past, we have proposed novel dual adaptive finite element based strategies for high resolution (around 1 mm) yet rapid (under 20 minutes) fluorescence optical tomography for large tissue volumes of approximately 1 liter.

A promising application of adaptive finite element-based fluorescence tomography is the identification of the lymph nodes draining from the primary tumor in breast cancer patients. Breast cancer predominantly spreads through the lymph system. Localization of small fluorescently tagged regions of cancerous tissue in the lymph nodes around the breast can guide the surgeon for resection. In addition, 3D imaging of cancerous tissue with suitably designed agents can also act as a tool for tracking the spread of the disease, and monitoring the response to therapy. In this article, we detail the development and implementation of an adaptive finite element based non-contact fluorescence tomography algorithm and demonstrate the 3D localization of fluorescently tagged targets in tissue from both synthetic and real experimental measurements acquired on physiological geometries.

1. Introduction

As near infrared (NIR) light can travel several centimeters in tissue, fluorescence enhanced NIR optical imaging promises to open new pathways for the characterization of biological processes in living animals at cellular and molecular levels. In the past decade, several approaches have been proposed for fluorescence enhanced optical tomography involving the determination of the fluorophore yield and/or fluorescence lifetime distribution in the tissue from a finite number of boundary measurements.

These approaches include perturbative localization [**16**, **30**, **39**], back-projection type methods [**24**–**26**, **37**], Born Approximation [**14**, **29**, **31**], random walk theory [**10**], and more recently, fast fluorescence localization [**33**]. Other researchers have cast the image reconstruction problem as an optimization problem in which a least squares type minimization is performed in order to determine the fluorescence map which best predicts the measured boundary fluorescence distribution. Optimization approaches are more general in their scope and can handle heterogeneous backgrounds as well as large sample volumes albeit at increased computational cost. Typically, Newton-type or conjugate gradient methods [**2**, **17**, **32**, **35**] have been employed to solve the optimization formulation of the problem, both in deterministic and in Bayesian frameworks [**11**–**13**, **27**].

The achievable resolution for fluorescence tomography is determined by multiple factors including the signal to noise ratio, target depth, and the level of discretization. Traditionally, the discretization level has been selected *a priori* based on knowledge of the domain and/or computational constraints. The image quality can often be improved by uniformly refining the level of discretization throughout the domain. However, this global refinement further increases the ill-posedness of the problem and quickly results in insurmountable computational requirements by increasing the number of unknowns. To avoid this problem, we have previously proposed adaptive finite element methods for reconstructing high resolution 3D fluorescence images by employing separate and independently evolving meshes for the forward and inverse problems arising in optical tomography and demonstrated resolution gains up to the mean transport length scales (approximately 1 mm) [**20**]. These algorithms were experimentally verified with frequency domain fluorescence measurements acquired on tissue-mimicking phantoms [**19**].

NIR fluorescence imaging is applicable to a number of applications, but lymph node tomography is a particularly promising area. The lymph system is thought to be responsible for the metastatic spread of cancer, and proximal lymph nodes are often resected in hopes to curb the spread of a tumor. Consequently, the development of a molecular imaging method for locating lymph nodes in 3-D can be a potent tool for diagnostics, image guided surgery, and monitoring response to cancer therapy. Optical agents such as fluorescent indocyanine green [**15**], quantum dots [**23**], and other organic dyes [**18**] have been shown to image lymph nodes in animals using planar imaging. While planar imaging is sufficient for qualitative studies, the development of a tomographic modality to locate molecular probe distribution in three dimensions is needed to

quantitatively track probe transport through the lymphatic system and for accurate image guided lymph node resection procedures.

As NIR light can not penetrate though the thickness of human or swine bodies, only reflectance measurements can be acquired. In prior work, we have demonstrated localization of fluorescent targets buried in homogeneous tissue-like media from frequency domain fluorescence measurements acquired with an area illumination and area detection system [**19**]. While sufficient for simple phantom experiments, measurements using only a single expanded laser excitation source can not successfully reconstruct multiple fluorescence targets buried in large heterogeneous volumes. We proposed and demonstrated the use of multiple spatially patterned excitation sources for tomography in resolving multiple fluorescence targets distributed in clinically relevant volumes in [**21**]. In this contribution, we demonstrate the use of such spatially patterned excitation sources for locating multiple fluorescent anomalies in tissue, using both simulated and real measurements on physiological swine bodies geometries captured by a stereo vision system.

The layout of this paper is as follows: In Section 2, we derive the formulation of and algorithms for multiple excitation based fluorescence tomography, as well as discuss its computational implementation. In Section 3, we briefly describe the synthetic and real experimental measurement configurations for frequency domain fluorescence imaging of swine and present image reconstruction examples. We conclude in Section 4 we summarize our work and point out implications and future directions.

2. Adaptive Fluorescence Tomography Algorithm

Fluorescence optical tomography is typically performed in a model-based framework, wherein a photon transport model is used to predict boundary fluorescence measurements for a given fluorescence absorption map in the tissue interior. The map of the absorption owing to fluorophore is then iteratively updated until the predicted measurements match the experimentally observed ones. For time-periodic sources modulated at a frequency ω, the following set of coupled photon diffusion equations accurately describes the complex-valued photon fluences $u = u(\mathbf{r})$ at the excitation wavelength and $v = v(\mathbf{r})$ at the fluorescent wavelength:

$$-\nabla \cdot [D_x(\mathbf{r})\nabla u(\mathbf{r})] + k_x u(\mathbf{r}) = 0, \tag{2.1}$$

$$-\nabla \cdot [D_m(\mathbf{r})\nabla v(\mathbf{r})] + k_m v(\mathbf{r}) = \beta_{xm} u(\mathbf{r}). \tag{2.2}$$

Here,

$$D_{x,m} = \frac{1}{3(\mu_{ax,mi} + \mu_{ax,mf} + \mu'_{sx,m})},$$

$$k_{x,m} = \frac{i\omega}{c} + \mu_{ax,mi}(\mathbf{r}) + \mu_{ax,mf}(\mathbf{r}), \qquad \beta_{xm} = \frac{\phi\mu_{axf}}{1 + i\omega\tau(\mathbf{r})}.$$

Subscripts x and m denote material properties at excitation and emission wavelengths, respectively: $D_{x,m}$ are the photon diffusion coefficients; $\mu_{ax,mi}$ the absorption coefficients due to endogenous chromophores; $\mu_{ax,mf}$ the absorption coefficients due to exogenous fluorophore; $\mu'_{sx,m}$ the reduced scattering coefficients; ϕ the quantum efficiency of the fluorophore; and finally, τ is the fluorophore lifetime associated with first order fluorescence decay kinetics. These equations are solved with Robin-type boundary conditions on the boundary $\partial\Omega$ of the domain Ω:

$$2D_x \frac{\partial u}{\partial n} + \gamma u + S(\mathbf{r}) = 0, \qquad 2D_m \frac{\partial v}{\partial n} + \gamma v = 0, \tag{2.3}$$

where n denotes the outward normal to the surface and γ is a constant depending on the optical reflective index mismatch at the boundary. The complex-valued function $S(\mathbf{r})$ is the excitation boundary source.

The goal of fluorescence tomography is to reconstruct the spatial map of coefficients $\mu_{axf}(\mathbf{r})$ and/or $\tau(\mathbf{r})$ from measurements of the emission fluence v on the boundary. In this work we focus on the recovery of only $\mu_{axf}(\mathbf{r})$. For notational brevity, we set $\mu_{axf} = q$ in the following paragraphs. The remaining optical properties were assumed known, with values corresponding to a 2% Liposyn solution [**19**].

In our imaging scheme, a laser shaped into a line profile is scanned across M positions on the tissue surface, representing sources $S^i(\mathbf{r}), i = 1, 2, \ldots, M$. For each source position, fluorescence measurements are taken on the illumination plane. The image reconstruction problem can then be posed as a constrained optimization problem wherein an L_2 norm-based error functional of the distance between boundary fluorescence measurements $\mathbf{z} = \{z^i, i = 1, 2, \ldots, M\}$ and predictions $\mathbf{v} = \{v^i, i = 1, 2, \ldots, M\}$ is minimized by variation of the parameter q. The diffusion model above connecting q and v^i is used as an explicit constraint. In a function space setting this minimization problem reads as:

$$\begin{aligned} \min_{q,\mathbf{u},\mathbf{v}} \quad & J(q, \mathbf{v}) \\ \text{subject to} \quad & A^i(q; [u^i, v^i])([\zeta^i, \xi^i]) = 0, \ i = 1, \ldots, M. \end{aligned} \tag{2.4}$$

Here, the error functional $J(q, \mathbf{v})$ incorporates a least square error term over the measurement part Γ of the boundary $\partial\Omega$ and a Tikhonov regularization term:

$$J(q, \mathbf{v}) = \sum_{i=1}^{M} \frac{1}{2} \left\| v^i - \sigma z^i \right\|_{\Gamma}^2 + \beta r(q). \tag{2.5}$$

The parameter σ models the relationship between actual fluorescent fluence at the tissue surface and the CCD camera signal. As the detector amplification and the laser diode power are typically kept constant for all M source positions, the same σ is used for all line source positions and is empirically determined. In practice fluorescence phase measurements are made relative to the excitation source S, hence σ can be treated as a real number since only the amplitude of the excitation source is treated as unknown. While σ can be efficiently fitted, in practice a constant value can be predetermined for fixed instrument gain settings. β is the Tikhonov regularization parameter.

The constraint $A^i(q; [u^i, v^i])([\zeta^i, \xi^i]) = 0$ is the weak or variational form of the coupled photon diffusion equations in frequency domain with partial current boundary conditions for the i^{th} excitation source, and with test functions $[\zeta, \xi] \in H^1(\Omega)$:

$$\begin{aligned} &A^i(q; [u^i, v^i])([\zeta^i, \xi^i]) = \\ &\quad (D_x \nabla u^i, \nabla \zeta^i)_\Omega + (k_x u^i, \zeta^i)_\Omega + \frac{\gamma}{2}(u^i, \zeta^i)_{\partial\Omega} + \frac{1}{2}(S^i, \zeta^i)_{\partial\Omega} \\ &\quad + (D_m \nabla v^i, \nabla \xi^i)_\Omega + (k_m v^i, \xi^i)_\Omega + \frac{\gamma}{2}(v^i, \xi^i)_{\partial\Omega} - (\beta_{xm} u^i, \xi^i)_\Omega. \end{aligned}$$

It is known that the solution of the constrained minimization problem (2.4) is a stationary point of the Lagrangian [**20**]

$$L(x) = J(q, \mathbf{v}) + \sum_{i=1}^{M} A^i(q; [u^i, v^i])([\lambda_i^{ex}, \lambda_i^{em}]). \tag{2.6}$$

Here, $\lambda_i^{ex}, \lambda_i^{em}$ are the Lagrange multipliers corresponding to the excitation and emission diffusion equation constraints for the i^{th} source, respectively, and we use the abbreviation $x = \{\mathbf{u}, \mathbf{v}, \boldsymbol{\lambda}^{ex}, \boldsymbol{\lambda}^{em}, q\}$ for brevity. The definition of a stationary point is that at this point, all derivatives with respect to its arguments are zero. For complex-valued functions, this means that both real and imaginary part of the derivative are zero. The stationary point is found using the Gauss-Newton method which computes an update direction $\delta x_k = \{\delta\mathbf{u}_k, \delta\mathbf{v}_k, \delta\boldsymbol{\lambda}_k^{ex}, \delta\boldsymbol{\lambda}_k^{em}, \delta q_k\}$ by solving the linear system

$$L_{xx}(x_k)(\delta x_k, y) = -L_x(x_k)(y) \qquad \forall y, \tag{2.7}$$

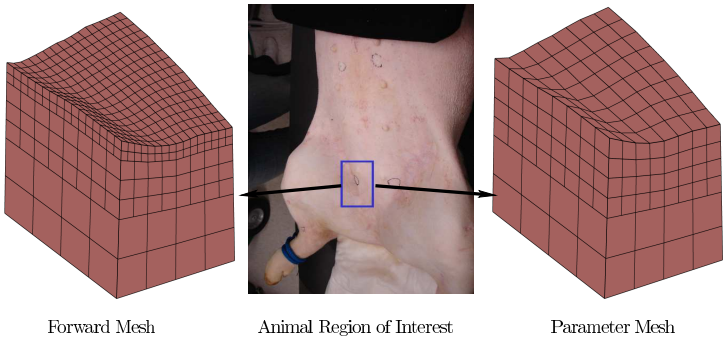

FIGURE 1. Geometry for the first numerical experiment. The animal surface in the groin region was characterized with a photogrammetric measurement and two coarse FE meshes were created for discretizing the forward/adjoint variables as well as the unknown parameter.

where $L_{xx}(x_k)$ is the Gauss-Newton approximation to the Hessian matrix of second derivatives of L at point x_k, and y are test functions. The norm of the first derivative of the Lagrangian, i.e. the residual of the optimality conditions $\|\nabla L\|$, is tracked to monitor the progress of the solution and it is used as one of the triggers of mesh refinement decisions [**4**, **5**].

Equations (2.7) are discretized by the finite element method. State and adjoint variables u^i, v^i, λ_i^{ex}, and λ_i^{em} for each excitation source are discretized and solved for on individual meshes with continuous finite elements, while the unknown parameter map q is discretized on a separate mesh with discontinuous finite elements. Hence for M sources, $M + 1$ finite element meshes are employed. These meshes are adaptively refined and fast Gauss-Newton updates to the unknown parameter map are calculated by carrying out the forward and adjoint computations corresponding to different sources in parallel. The mesh adaptation criteria and the parallelized Gauss-Newton update strategy is detailed in Ref. [**21**]. The computations were implemented using the Open Source finite element library deal.II [**6**]. More details can be found in References [**4**, **5**, **7**].

3. Image Reconstruction Examples

Here, we present image reconstructions from numerical experiments employing both synthetically generated and real measurement data to demonstrate the utility and efficiency of the techniques described in the previous section for practical lymph node imaging.

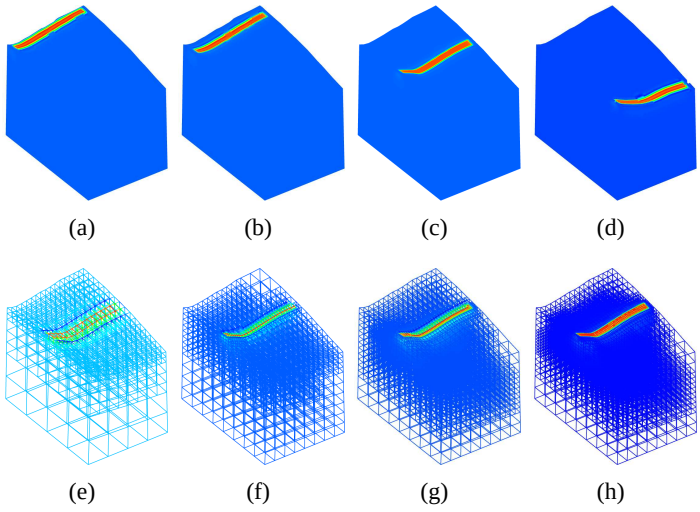

FIGURE 2. Scanning line source simulation setup for the first numerical experiment: (a-d) 1st, 2nd, 8th and 16th source locations. (e-f) Evolution of the state mesh for the 8th source.

Example 1. In the first example, we employ a geometry extracted with photogrammetric techniques from the region of a swine's groin, see Fig. 1. A 10.8cm $\times$ 7.4cm $\times$ 9.1cm box was projected to the acquired geometry to form our computational domain. We then generated synthetic measurement data corresponding to three embedded 5mm fluorescence targets containing 1μM of Indocyanine Green (ICG) dye solution. ICG excites in a wavelength band around 785nm and emits around 830nm. To generate the synthetic data, a 785nm laser line source (2mm wide, 6cm long) was simulated to scan across the tissue surface, see Fig. 2a–d, and fluorescence amplitude and phase at the illumination surface were computed for each of $M = 16$ source positions.

The two initial meshes shown in Fig. 1 were prepared to start the image reconstruction iterations. The state mesh was refined according to a Kelly-type error indicator [**38**] for the state $\mathbf{u}, \mathbf{v}$ and adjoint variables $\lambda^{\mathbf{ex}}, \lambda^{\mathbf{em}}$. Fig.s 2(e-f) show several iterations of the state mesh evolution for the 8th source position. Similar meshes were generated in parallel for the other source positions. The unknown parameter $q = \mu_{axf}(\mathbf{r})$ was discretized on a sequence of coarser meshes.

Using these succesions of meshes, we performed Gauss-Newton updates. For this example, no further progress in the image reconstruction

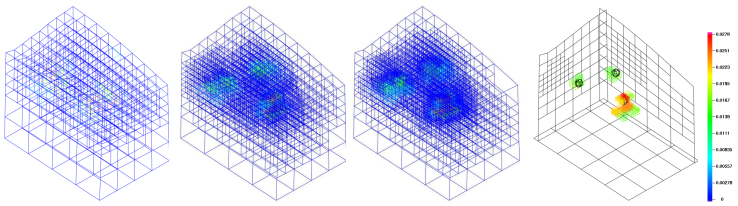

(a) (b) (c) (d)

FIGURE 3. (a-c) Parameter mesh evolution for the reconstruction of three fluorescence targets. (d) Those cells where $q_k(\mathbf{r}) \geq 50\% \max_{\mathbf{r}' \in \Omega} q_k(\mathbf{r}')$ are shown as blocks, whereas the actual location and size of the targets are drawn as spheres. In addition, the mesh on three cut planes through the domain is shown.

was achieved after 6 adaptive mesh refinements and a total of 29 iterations. Fig.s 3a–c indicate the parameter mesh evolution. Fig. 3d illustrates the recovered fluorescent targets. True target locations and sizes are shown as black wireframes. True and recovered target locations coincide. However, the recovered magnitude of reconstructed fluorescence absorption is lower than the true level of 0.598cm^{-1}, primarily because of the smoothing effect of Tikhonov regularization; furthermore, the recovered $\mu_{axf}(\mathbf{r})$ values differ in the three targets owing to different reconstruction sensitivities at different depths from the illumination/detection surface.

Example 2. In our second example, we demonstrate inversion of real experimental measurements. To acquire the measurements, a live and anesthetized Yorkshire Swine was injected with a lymph targeting fluorescent contrast agent. Measurements corresponding to 6 line sources positioned symmetrically about the suspected lymph node location (as ascertained from 2-D images) were employed. Fig. 4 shows four of the raw measurement datasets at excitation and emission wavelengths. The excitation wavelength images illustrate the scanning line source; these images were used to construct the source term $S(\mathbf{r})$ for the boundary condition (2.3). The emission amplitude and phase images constituted the boundary measurements used in the inversion for the parameter $q = \mu_{axf}(\mathbf{r})$. More details about the experimental configuration can be found in Ref.s [**19**, **34**].

A cubical region of roughly $(8\text{cm})^3$ around the suspected node location was used as the measurement and image reconstruction volume. Forward and adjoint variables where initially discretized on meshes with cell sizes of 1cm, while for the unknown image the initial mesh resolution

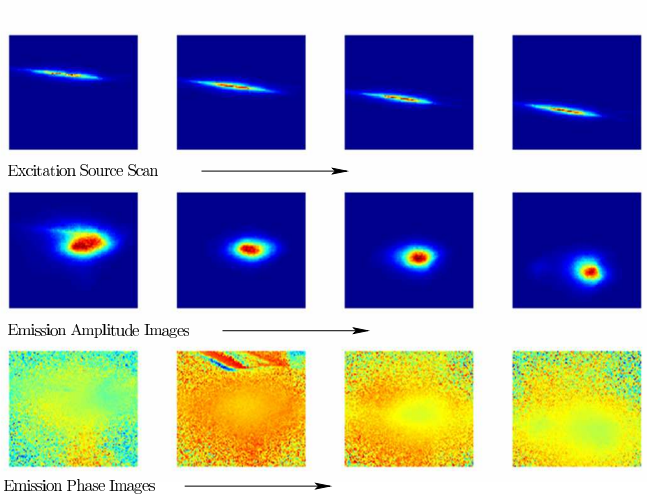

FIGURE 4. Real measurement data at the illumination and detection surface. Top row: Excitation wavelength images of the scanning line source. Middle row: Corresponding fluorescence emission amplitude images. Bottom row: Associated fluorescence phases.

was 2cm. As the Gauss-Newton parameter update iterations proceeded, the mesh refinement algorithm produced grids that for forward/adjoint computations better resolve the laser line source and accurately solve the photon diffusion equations, while the parameter mesh increasingly better delineated the target and became coarser in regions away from the suspected target location. No further image update was obtained after 26 Gauss-Newton iterations during which 7 automatic mesh refinements/derefinements were triggered.

Fig. 5a depicts the mesh used to discretize the parameter after the final refinement step. Fig. 5b shows only those cells where the reconstructed parameter exceeds 50% of its maximum. The depth of the reconstructed targets (lymph nodes in this case) was estimated to be $3cm$; this agreed with the observation of the surgeon that the resected lymph node in the imaged location was $3 - 3.5cm$ deep.

Computational considerations. The linear Karush-Kuhn-Tucker, or KKT, system resulting from the discretization of the Newton update (2.7) can rapidly become quite large (hundreds of thousands to millions of unknowns) for the case of multiple excitation source measurements. Hence, it is essential that the image reconstruction process be started from coarse

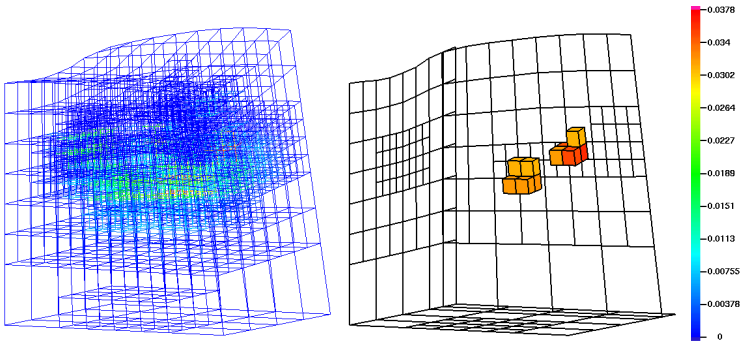

(a) (b)

FIGURE 5. Lymph node image reconstruction from experimental measurements. (a) Final adaptively refined parameter mesh. (b) Cells where the reconstructed parameter is larger than 50% of its maximum. In addition, the mesh on three cut planes through the domain is shown.

state and parameter meshes. Fig. 6a–b shows the growth in the global number of unknowns and the number of parameter unknowns as Gauss-Newton iterations progress for the two numerical experiments described above. The total size of the system exceeds one million by the end of the reconstruction process; however, we are able to keep the compute time within 20-25 minutes by distributing computations onto different nodes of a Beowulf cluster computer.

Fig. 6c–d illustrates the decrease in data misfit $\sum_{i=1}^{M} \frac{1}{2} \left\| v^i - \sigma z^i \right\|_{\Gamma}^2$ and the residual of the first order optimality condition $\|L_x(x)\|$ as iterations pregress. As described in [7], the regularization parameter β is adjusted after each iterations to avoid that the regularization term dominates the misfit term. Most of the decrease in the data misfit and the residual is obtained in the initial few iterations on the coarse meshes, however the images keep on improving in terms of target location accuracy along with adaptive mesh refinements in succeeding iterations.

4. Conclusions

In this contribution, we briefly reviewed the adaptive finite element method approach to fluorescence optical tomography, a rapidly growing biomedical imaging modality that is currently undergoing its first clinical studies. Uniformly refined meshes can not deliver clinically necessary resolutions because they lead to nonlinear optimization problems that are

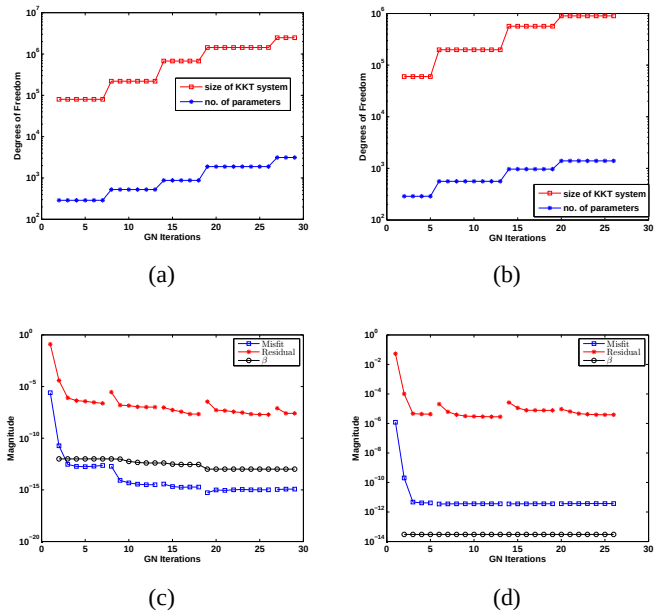

FIGURE 6. Progress of computations for examples 1 (left) and 2 (right column) as Gauss-Newton iterations progress. (a-b) Increase in the size of linear KKT system (i.e. the number of global degrees of freedom) and the number of unknowns to discretize the parameter $q(\mathbf{r})$. (c-d) Reduction in data misfit $\sum_{i=1}^{M} \frac{1}{2} \left\| v^i - \sigma z^i \right\|_{\Gamma}^2$ and residual of the first order optimality condition $\|L_x(x)(y)\|$, as well as our choice of the Tikhonov regularization parameter β in each iteration.

orders of magnitude too large for today's hardware to solve within clinically acceptable time scales. Our solution to this problem was the introduction of adaptively refined meshes for solving the forward/adjoint problems and the unknown parameter updates. They not only are able to focus numerical effort to regions in the domain where high resolution is actually necessary, but also regularize the inverse problem and in particular make the initial Gauss-Newton iterations extremely rapid since we can compute on coarse meshes while we are still far away from the solution.

Using multiple excitation source patterns is essential for acquiring high information content measurements of tissue with non-contact instrumentation setups. We have integrated a multiple experiment inversion approach with the adaptive tomography algorithm which exploits the availability of multiprocessor computers and Beowulf clusters to rapidly solve the scanning excitation source tomography problem. Finally, we demonstrated the application of the developed algorithms and methods to the important clinical problem of locating lymph nodes marked with fluorescent contrast agents with realistic geometries and with experimental measurements. Multiple fluorescent targets can be identified with only reflectance mode measurements through the judicious use of scanning excitation source patterns. In this manuscript we focused only on the recovery of fluorescent target locations by recovering $\mu_{axf}(\mathbf{r})$ maps. However, in case the lifetime $\tau(\mathbf{r})$ of the fluorophore is also spatially varying and unknown, then a sequential update strategy which alternates the update of $\mu_{axf}(\mathbf{r})$ with the update in $\tau(\mathbf{r})$ or $\beta_{xm}(\mathbf{r})$ is needed.

Although we are able to efficiently solve inverse fluorescence tomography problem with practically sufficient resolution, we believe that further progress is necessary in a number of areas to improve the numerical performance. The linear solvers spend 75% of the compute time on fine meshes. It is therefore important to think about viable ways to precondition the solution of state/adjoint and parameter updates. One approach would be to use BFGS or LM-BFGS approximations [**28**] of the Schur complement of the KKT system arising from the discretization of the equation (2.7) as used in [**8**]. However, BFGS methods would have to be integrated with adaptivity since current quasi-Newton implementations expect the parameter space to remain fixed. Another approach is to use multilevel algorithms for the Schur complement or the whole KKT system. Methods in this direction have already been explored in [**1**, **3**, **9**, **22**]. Numerical methods do not only have to work in simple situations like the ones shown in Section 3, but also in the presence of significant background heterogeneity, unknown or large noise levels, systematic measurement bias, and other practical constraints. Systematic testing of reconstructions for statistically sampled scenarios with Objective Assessment of Image Quality (OAIQ) methods [**36**] will be necessary to achieve clinical recognition for fluorescence optical tomography.

Acknowledgments

Part of this work was supported by NIH grant R01 CA 67176. The authors acknowledge the assistance of Dr. John Rasmussen in the Division

of Molecular Imaging at the Baylor College of Medicine, where the experimental measurements used in the numerical examples were obtained. Dr. Wei Wang, also from the Division of Molecular Imaging provided the lymph targeting fluorescent contrast agent, and Dr. Shi Ke performed the dye injections.

References

1. S. S. Adavani and G. Biros, *Multigrid algorithms for inverse problems with linear parabolic PDE constraints*, submitted (2007).
2. S. R. Arridge, *Image reconstruction in optical tomography*, Philosophical Transactions: Biological Sciences **352** (1997), no. 1354, 717–726.
3. U. M. Ascher and E. Haber, *A multigrid method for distributed parameter estimation problems*, ETNA **15** (2003), 1–12.
4. W. Bangerth, *Adaptive finite element methods for the identification of distributed parameters in partial differential equations*, Ph.D. thesis, University of Heidelberg, 2002.
5. _____, *A framework for the adaptive finite element solution of large inverse problems*, SIAM J. Sc. Comput. (2007), accepted.
6. W. Bangerth, R. Hartmann, and G. Kanschat, *deal.II – a General Purpose Object Oriented Finite Element Library*, ACM Trans. Math. Softw. **33** (2007), 24/1–24/27. See also `http://www.dealii.org/`.
7. W. Bangerth and A. Joshi, *Adaptive finite element methods for the solution of inverse problems in optical tomography*, Inverse Problems (2007), submitted.
8. G. Biros and O. Ghattas, *Parallel Lagrange-Newton-Krylov-Schur methods for PDE-constrained optimizaion. Part I: The Krylov-Schur solver*, SIAM J. Sci. Comput. **27** (2005), 687–713.
9. A. Borzì, K. Kunisch, and D. Y. Kwak, *Accuracy and convergence properties of the finite difference multigrid solution of an optimal control problem*, SIAM J. Control Optim. **41** (2003), 1477–1497.
10. V. Chernomordik, D. Hattery, I. Gannot, and A. H. Gandjbakhche, *Inverse method 3-D reconstruction of localized in vivo fluorescence-application to Sjøgren syndrome*, IEEE J. Sel. Top. Quantum Electron. **54** (1999), 930–935.
11. M. J. Eppstein, D. E. Dougherty, T. L. Troy, and E. M. Sevick-Muraca, *Biomedical optical tomography using dynamic parametrization and Bayesian conditioning on photon migration measurements*, Appl. Opt. **38** (1998), no. 10, 2138–2150.
12. M. J. Eppstein, D. J. Hawrysz, A. Godavarty, and E. M. Sevick-Muraca, *Three dimensional near infrared fluorescence tomography with Bayesian methodologies for image reconstruction from sparse and noisy data sets*, Proc. Nat. Acad. Sci. **99** (2002), 9619–9624.
13. A. Godavarty, M. J. Eppstein, C. Zhang, S. Theru, A. B. Thompson, M. Gurfinkel, and E. M. Sevick-Muraca, *Fluorescence-enhanced optical imaging in large tissue volumes using a gain-modulated ICCD camera*, Phys. Med. Biol. **48** (2003), 1701–1720.
14. E. E. Graves, J. Ripoll, R. Weissleder, and V. Ntziachristos, *A submillimeter resolution fluorescence molecular imaging system for small animal imaging*, Med. Phys. **30** (2003), 901–911.

15. M. Gurfinek, A. B. Thompson, J. Reynolds, E. M. Sevick-Muraca, et al., *Pharmacokinetics of ICG and HPPH-car for the detection of normal and tumor tissue using fluorescence, near-infrared reflectance imaging: a case study*, Photochem. Photobiol. (2000).
16. E. L. Hull, M. G. Nichols, and T. H. Foster, *Localization of luminescent inhomogeneities in turbid media with spatially resolved measurements of CW diffuse luminescence emittance*, Appl. Opt. **37** (1998), 2755–2765.
17. H. Jiang, *Frequency-domain fluorescent diffusion tomography: A finite element based algorithm and simulations*, Appl. Opt. **37** (1998), no. 22, 5337–5343.
18. L. Josephson, U. Mahmood, P. Wunderbaldinger, Y. Tang, and R. Weissleder, *Pan and sentinel lymph node visualization using a near-infrared fluorescent probe*, Mol. Imaging (2003).
19. A. Joshi, W. Bangerth, K. Hwang, J. Rasmussen, and E. M. Sevick-Muraca, *Fully adaptive FEM based fluorescence optical tomography from time-dependent measurements with area illumination and detection*, Med. Phys. **33** (2006), no. 5, 1299–1310.
20. A. Joshi, W. Bangerth, and E. M. Sevick-Muraca, *Adaptive finite element modeling of optical fluorescence-enhanced tomography*, Optics Express **12** (2004), no. 22, 5402–5417.
21. ———, *Non-contact fluorescence optical tomography with scanning area illumination*, Proceedings of the IEEE International Symposium on Biomedical Imaging, Arlington, VA, 2006, IEEE, 2006, pp. 582–585.
22. B. Kaltenbacher, *On the regularization properties of a full multigrid method for ill-posed problems*, Inverse Problems **17** (2001), 767–788.
23. S. Kim, Y. T. Lim, E. G. Soltesz, J. Lee A. M. De Grand, A. Nakayama, J. A. Parker, T. Mihaljevic, R. G. Laurence, D. M. Dor, L. H. Cohn, M. G. Bawendi, and J. V. Frangioni, *Near-infrared fluorescent type II quantum dots for sentinel lymph node mapping*, Nature Biotechnology **22** (2004), 93–97.
24. V. A. Markel, V. Mital, and J. C. Schotland, *Inverse problem in optical diffusion tomography. III. Inversion formulas and singular-value decomposition*, Journal of the Optical Society of America A **20** (2003), no. 5, 890–902.
25. V. A. Markel, J. A. O'Sullivan, and J. C. Schotland, *Inverse problem in optical diffusion tomography. IV. Nonlinear inversion formulas*, Journal of the Optical Society of America A **20** (2003), no. 5, 903–912.
26. V. A. Markel and J. C. Schotland, *Inverse problem in optical diffusion tomography. I. Fourier-Laplace inversion formulas*, Journal of the Optical Society of America A **18** (2001), no. 6, 1336–1347.
27. A. B. Milstein, S. Oh, K. J. Webb, C. A. Bouman, Q. Zhang, D. Boas, and R. P. Milane, *Fluorescence optical diffusion tomography*, Appl. Opt. **42** (2003), no. 16, 3061–3094.
28. J. Nocedal and S. J. Wright, *Numerical optimization*, Springer Series in Operations Research, Springer, New York, 1999.
29. V. Ntziachristos and R. Weissleder, *Experimental three-dimensional fluorescence reconstruction of diffuse media by use of a normalized Born approximation*, Opt. Lett. **26** (2001), no. 12, 893–895.
30. M. A. O'Leary, D. A. Boas, B. Chance, and A. G. Yodh, *Reradiation and imaging of diffuse photon density waves using fluorescent inhomogeneities*, J. Luminescence **60** (1994), 281–286.

31. _____, *Fluorescence lifetime imaging in turbid media*, Opt. Lett. **20** (1996), 426–428.
32. D. Y. Paithankar, A. U. Chen, B. W. Pogue, M. S. Patterson, and E. M. Sevick-Muraca, *Imaging of fluorescent yield and lifetime from multiply scattered light reemitted from random media*, Appl. Opt. **36** (1997), no. 10, 2260–2272.
33. H. Quan and Z. Guo, *Fast 3-D optical imaging with transient fluorescence signals*, Opt. Express **12** (2004), no. 3, 449–457.
34. J. S. Reynolds, T. L. Troy, and E. M. Sevick-Muraca, *Multi-pixel techniques for frequency-domain photon migration imaging*, Biotechnolgy Progress **13** (1997), 669–680.
35. R. Roy and E. M. Sevick-Muraca, *Truncated Newton's optimization schemes for absorption and fluorescence optical tomography: Part(1) theory and formulation*, Opt. Express **4** (1999), no. 10, 353–371.
36. A. Sahu, A. Joshi, M. Kupinsky, and E. M. Sevick-Muraca, *Assessment of a fluorescence enhanced optical imaging system using the Hotelling observer*, Optics Express **14** (2006), no. 17, 7642–7660.
37. J. C. Schotland, *Continuous wave diffusion imaging*, J. Opt. Soc. Am. A **14** (1997), 275–279.
38. D. W.Kelly, S. R.J. P. Gago, O. C Zienkiewicz, and I. Babuska, *A posteriori error analysis in finite element method: Part ii–adaptive mesh refinement*, Int. J. Numer. Math. Eng **19** (1983), 1621–1656.
39. J. Wu, Y. Wang, L. Perleman, I. Itzkan, R. R. Desai, and M. S. Feld, *Time resolved multichannel imaging of fluorescent objects embedded in turbid media*, Opt. Lett. **20** (1995), 489–491.

DEPARTMENT OF RADIOLOGY, BAYLOR COLLEGE OF MEDICINE, HOUSTON, TX 77030, USA

E-mail address: amitj@bcm.edu

DEPARTMENT OF MATHEMATICS, TEXAS A&M UNIVERSITY, COLLEGE STATION, TX 77843, USA

E-mail address: bangerth@math.tamu.edu